Journal of Sailing Technology 2024, volume 9, issue 1, pp. 19 - 41.
The Society of Naval Architects and Marine Engineers.

Fluid-Structure Interactions Response of a Composite Hydrofoil Modelled With 1D Beam Finite Elements

Antoine Faye
Naval Academy Research Institute, France, antoine.faye@ecole-navale.fr.

Paolo Perali
ENSTA Bretagne, France.

Benoit Augier
IFREMER, France.

Matthieu Sacher
ENSTA Bretagne, France.

Jean-Baptiste Leroux
ENSTA Bretagne, France.

Alain Nême
ENSTA Bretagne, France.

Jacques-André Astolfi
Naval Academy Research Institute, France.

Manuscript received November 20, 2023; revision received March 5, 2024; accepted March 21, 2024.

Abstract. In this paper, the hydroelastic response of a NACA0015 composite hydrofoil is studied experimentally and numerically. The foil is made of composite materials with fibers not aligned with the span of the foil, which results in the occurence of a bend-twist coupling in the material. Computations are performed using a partitioned approach. The flow problem is solved using a boundary element method. The structural response of the foil is modelled with two different finite element models. In the first one, the foil is modelled with 2D shell and 3D solid finite elements and in the second model, the foil is modelled with 1D beam finite elements. The experiments are conducted in an open circulation water channel. Hydrodynamic forces and structural displacements are measured for several angles of attack, free stream velocities and submergence depth. This paper shows that the mechanical behaviour of a composite hydrofoil submitted to hydrodynamic loads can be modelled with 1D beam finite elements. This model gives results very similar to a finite element analysis realized with 2D shell and 3D solid finite elements, which are commonly used to model composite structures. The present work also shows that the experimental results can be well predicted by numerical simulations, but it requires a precise modeling of the bend-twist coupling in the materials constituting the foil.

Keywords: Hydrofoil; Equivalent Beam; Fluid-Structure Interactions; Composite; Bend-Twist Coupling.

NOMENCLATURE

c	Chord of the foil [m]
C_l	Lift force coefficient [-]
E_l, E_t	Young modulus along longitudinal and transversal directions [Pa]
$\boldsymbol{F}$	Concentrated force to project on a beam element [N]
$\boldsymbol{F_1}$,$\boldsymbol{F_2}$	Nodal forces to apply to the nodes of a beam element [N]
F_I^t	Hydrodynamic forces magnitude acting on the foil at a given iteration [N]
g	Average gravitational pull of the Earth [m.s^{-2}]
G_{lt}, G_{lf}, G_{tf}	Shear modulus [Pa]
h	Immersion of the foil [m]
I	Number the current iteration [-]
$I_{\min}$	Minimal number of iterations for a FSI simulation [-]
K	Timoshenko stiffness matrix of a section [N;N.m;N.m^2]
$\boldsymbol{M_1}$,$\boldsymbol{M_2}$	Nodal moments to apply to the nodes of a beam element [N]
$\boldsymbol{n}$	Outward pointing unit vector[-]
S	Timoshenko compliance matrix of a section [N^{-1};N^{-1}.m^{-1};N^{-1}.m^{-2}]
S_H	Hydrofoil boundary surface [-]
S_{FS}	Free surface boundary [-]
S_W	Wake boundary surface [-]
t	time [s]
$\boldsymbol{u}$	Velocity field computed [m.s^{-1}]
U	Flow speed [m.s^{-1}]
$\boldsymbol{U_0}$	Undisturbed flow velocity [m.s^{-1}]
u_I^{tip}	Displacement magnitude of the tip of the foil at a given iteration [m]
x,y	2D coordinates of the shear center of cross-section [m]
$\boldsymbol{x}$	Position vector of a point [m]
z	Spatial vertical coordinate [m]
Z	Distance to the heel of the foil [m]
α	Angle of attack [deg.]
β	Value of the Bend-Twist Ratio [deg./m]
β_{exp}	Value of the Bend-Twist Ratio computed experimentally [deg./m]
ϵ_s	Structural convergence criteria [m]
ϵ_f	Fluid convergence criteria [N]
η	Free surface elevation [m]
ν	Poisson coefficient [-]
ξ	Curvilinear abscissa of an arbitrary point of a beam element [-]
ρ	Density [kg/m^3]
ϕ	Disturbance potential [m.s^{-2}]
BEM	Boundary Element Method
BTC	Bend-Twist Coupling
BTR	Bend-Twist Ratio
FEA	Finite Element Analysis
FEM	Finite Element Method
$\mathrm{N_1}$,$\mathrm{N_2}$	Nodes of a beam element
QS	Quasi-Static
UD	Unidirectional
$\mathrm{X_l}$	Point of application of a concentrated force
$\mathrm{X_p}$	Point of application of a concentrated force projected on a beam element

1 INTRODUCTION

In high performances racing yacht design, hydrofoils are becoming more and more common. Thus, more studies to predict their performance are realized (Patterson and Binns, 2022; Graf et al., 2021; Patterson and Binns, 2022). For some foils, the hydrodynamic forces induce deformations which can not be neglected. In this case, Fluid-Structure Interactions (FSI) computations are realized to correctly predict their performance (Temtching Temou, 2020; Liao et al., 2019a; Marimon Giovannetti et al., 2022).

In the present work a partitioned approach is used. The hydrodynamic loads are obtained using the BEM code *PUFFIn*. The elastic deformation of the foil is computed with the finite element method (FEM), as implemented in *Abaqus™2022*. Classically, the finite elements used to describe composite hydrofoils are 2D shell elements or 3D solid elements (Liao et al., 2019a; Liao et al., 2019b; Temtching Temou, 2020; Mohammed Arab, 2020; Liao et al., 2021; Liao et al., 2023). In this work, 1D beam finite elements are considered, which allows a significant computational time reduction. Faye et al. (2022) shows that a 1D Finite Element Analysis (FEA) is approximately 250 times faster than a 3D FEA. Composite hydrofoils are characterized by anisotropic layup properties. Depending on the fiber orientation in the composite material, couplings between displacements and rotations may be present. For instance, the Bend-Twist Coupling (BTC) has a significant impact on the flow incidence seen by a hydrofoil submitted to a hydrodynamic loading (Lottati, 1985; Temtching Temou, 2020). An important BTC can lead to accelerated stall and static divergence (Young et al., 2017). Modelling foils with 1D beam elements allows to rapidly test several designs of foils to avoid such phenomenons. Inversely, numerical models could also be used to design self-regulating foils, where their angles of attack would be regulated by their deformations and BTC. By doing so, the velocity range where the foils are efficient would be maximized.

To describe the hydroelastic behavior of a foil with 1D beam finite elements, the three-dimensional geometric nonlinear equilibrium analysis of the foil is split into a linear one-dimensional analysis and a set of two dimensional linear analyses of the cross sections of the foil (Hodges, 2006). During the section analysis, 1D structural properties equivalent to the 3D model of the foil are determined. Then, these properties are used to perform the 1D FEA.

The experimental setup and hydrofoil properties are first presented in Section 2. Then, Section 3 details the numerical methods used to model the hydroelastic behaviour of the foil in a flow. Finally, Section 3 discusses the results obtained numerically and experimentally.

2 EXPERIMENTAL SETUP

2.1 Considered Foil

The studied foil is straight and prismatic, and its geometry is a NACA0015 section (chord c of 25 cm) extruded over 1.375 m. The dimensions of the foil are detailed in Table 1. The foil is composed of an Airex web foam, a ply of glass-epoxy taffeta and a unidirectional (UD) glass-epoxy ply. The taffeta ply behavior is assumed to be orthotropic with 1 and 2 directions respectively parallel to the warp and weft directions. For the UD ply, a transverse isotropic behavior is assumed, with the 1 direction parallel to the fiber. If an angle of 0° is assumed for the UD, the 1 directions of the UD and taffeta ply are aligned with the span of the foil. In this work, the orientation of the taffeta ply is fixed at 0°, thus its 1 direction is always aligned with the span of the foil. The cross section of the foil is illustrated in Figure 1 and the engineering elastic constants of the materials constituting the foils are presented in Tables 2, 3.

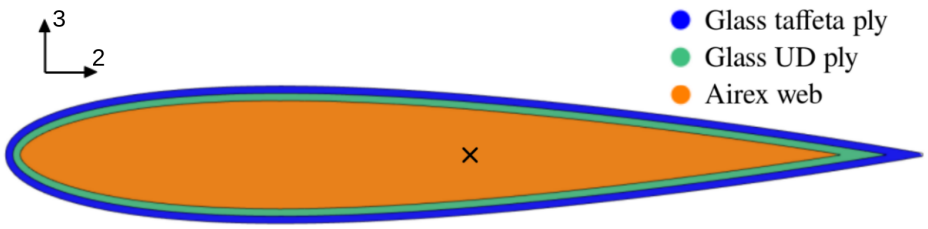

Figure 1. Cross section of the foil.

Figure 2 shows the studied foil, with a orange color mark to symbolize the orientation of the fibers in the UD ply. The angle between the leading edge of the foil and the fibers is -30°. Because the fibers are not aligned with the span of the foil, there is a bend-twist coupling in the foil. The BTC leads to a nose-up twist angle. When the foil is bent by the hydrodynamic loading, the nose-up twist angle increases its angle of attack (α) with respect to the flow. Therefore, the hydrodynamic loads of the foil increases when it is deformed.

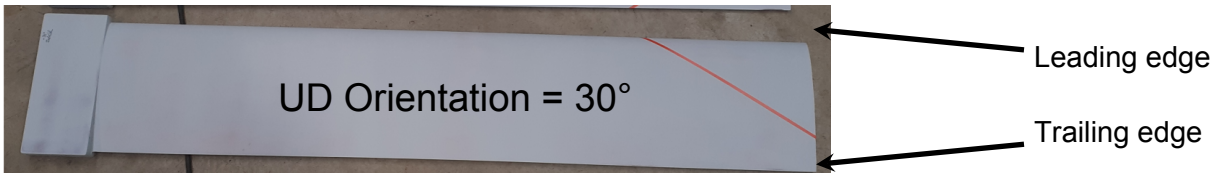

Figure 2. Considered hydrofoil.

Table 1. Geometric properties of the foils.

Chord (m)	Span (m)	Taffeta ply thickness (mm)	UD ply thickness (mm)	UD Orientation (deg)
0.250	1.375	9.45×10^{-2}	3.27×10^{-1}	-30

Table 2. Engineering constants of the materials constituting the skin of the foils.

Material	E_1 (GPa)	E_2 (GPa)	ν_{12}	G_{12} (GPa)	G_{13} (GPa)	G_{23} (GPa)	ρ (kg/m^3)
Taffeta	16.0	16.5	0.108	1.81	0.9	0.9	1625
UD	27.4	5.1	0.348	1.81	1.81	0.9	1625

Table 3. Mechanical properties of the Airex web.

Material	E (MPa)	ν	ρ (kg/m^3)
Airex Foam	25.0	0.400	60

2.2 Ifremer Flume Tank

The experimental campaign is realised at the current circulating tank of Ifremer, located in Boulogne-sur-Mer (France). The flume tank, illustrated in Figure 3, is 18 m long, 4 m wide and 2 m high. It generates a current, considered uniform, with velocities ranging from 0.1 m/s to 2.2 m/s. In the present study, the considered velocities U are 0.8 m/s and 1.2 m/s, respectively associated to Froude numbers of 0.51 and 0.77, considering the chord of the profile as the reference length. The turbulence intensity of the flow is considered constant with a value of 1.5%.

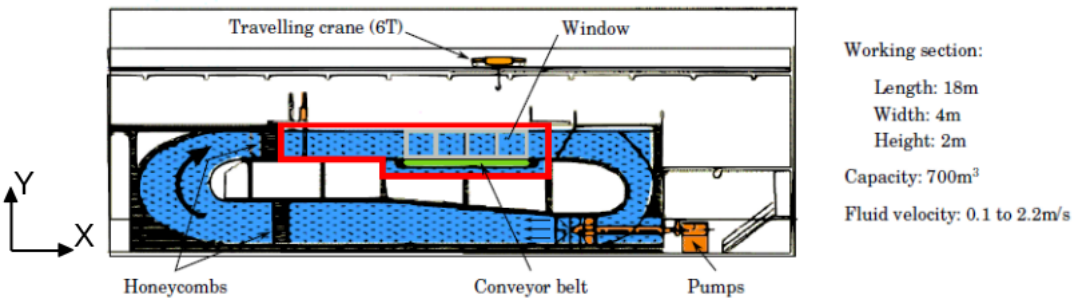

Figure 3. Scheme of the Ifremer Flume Tank, adapted from (Marty et al., 2021).

To ensure significant deformations of the foil, it is tested in the tank as a cantilever foil. It is fixed in a clamping system and a 6-DOF hexapod allows to change the angle of attack α and the immersion of the foil h. The rotation axis and reference point for the immersion are located at midchord of the non-deformed hydrofoil.

The hydrodynamic loads acting on the foil are measured with a balance fixed at the hexapod. The balance measures the three orthogonal force and moment components, respectively with a range of 150 DaN and 100 DaN.m. The precision of the balance is about 1.5 N for the forces and 1 N.m for the moments. To measure only the forces acting on the hydrofoil, the forces measured with the clamping system alone are substracted from the measurements. With this protocol, the hypothesis is made to neglect the foil-strut interaction. Considering this method, the clamping system is not modeled in *PUFFIn*.

As shown on Figure 4, a laser sheet is used to illuminate a section of the foil located at 1.19 m from the clamping. Images of the illuminated section are recorded using a high speed camera for the different angles of attack, immersion depths and flow velocity. Assuming that the foil section undergoes rigid displacements and rotations, an edge detection algorithm and a least square interpolation allow to get the positions of the section in the vertical plane. Substracting the position of the section at rest, it is finally possible to estimate the bending displacements and twist angles due to the hydrodynamic loads.

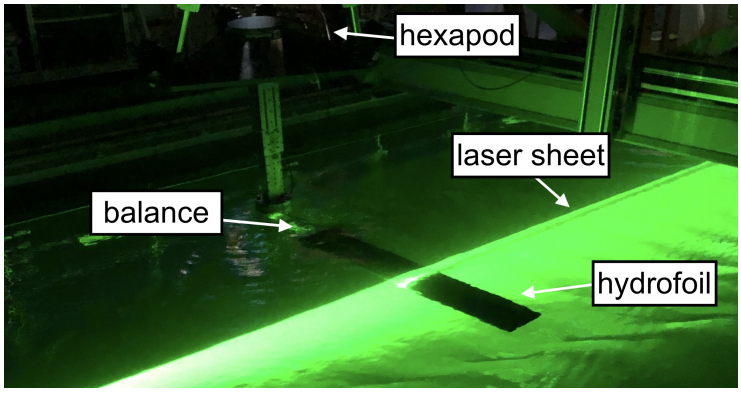

Figure 4. Laser sheet projected on the cantilever foil viewed at the top of the flume tank.

3 NUMERICAL MODELS

3.1 Flow Model

In this section, a brief description of the fluid solver *PUFFIn* is proposed. The fluid problem is solved with a Boundary Element Method (BEM) for potential flow. The viscous effects are neglected and the

flow is supposed to be irrotational and incompressible. The velocity field $\boldsymbol{u}(\boldsymbol{x},t)$ is the superposition of the undisturbed flow $\boldsymbol{U}_0$ and the gradient of a disturbance potential $\phi(\boldsymbol{x},t)$ satisfying a Laplace equation:

$$\Delta\phi(\boldsymbol{x},t) = 0. \tag{1}$$

Using the second Green identity, this equation is equivalent to a boundary integral equation on the domain boundaries (Katz and Plotkin, 2001), i.e. of the hydrofoil surface S_H, the free surface boundary S_{FS} and the wake surface S_W. These surfaces are represented in Figure 5 where η is the free surface elevation and c the chord of the hydrofoil:

$$\phi = \frac{1}{4\pi}\int_{S_H+S_{FS}} \left[\frac{\partial\phi}{\partial n}\frac{1}{r} - \phi\frac{\partial}{\partial n}\left(\frac{1}{r}\right)\right] \mathrm{d}S - \frac{1}{4\pi}\int_{S_W}\left[\phi\frac{\partial}{\partial n}\left(\frac{1}{r}\right)\right]\mathrm{d}S, \tag{2}$$

with $\boldsymbol{n}$ the outward pointing normal vector. Additional boundary conditions are needed to solve the boundary integral equation. On the hydrofoil, the non-penetration condition imposes:

$$\frac{\partial\phi}{\partial n} = \boldsymbol{U}_0 \cdot \boldsymbol{n}. \tag{3}$$

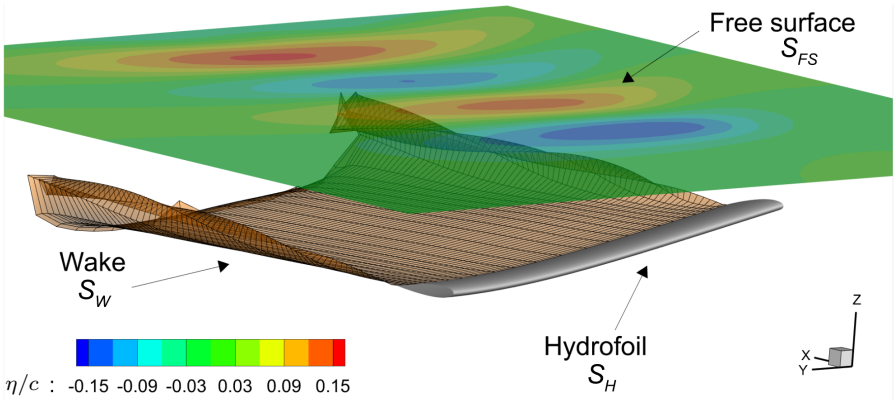

Figure 5. Boundary surfaces of the potential flow problem.

In addition, the linearized condition of Neumann-Kelvin (Newman, 2018) is imposed on the undisturbed free surface location ($z = 0$):

$$(\boldsymbol{U_0}\cdot\boldsymbol{\nabla})^2\,\phi + g\frac{\partial\phi}{\partial z} = 0. \tag{4}$$

The free surface elevation is obtained from the Bernoulli relation on the initial free surface:

$$\eta = -\frac{\boldsymbol{U_0}\cdot\boldsymbol{\nabla}\phi}{g}. \tag{5}$$

A Lagrangian approach is used to iteratively construct the wake surface during the computation. For inviscid flow, the potential on a wake panel convected by the flow should remain constant. Thus, the distribution of the potential ϕ on the wake can be obtained using a Kutta condition, imposing the equality of the extrados and intrados pressure at the trailing edge.

To construct a numerical solution, the boundaries are discretized using quadrilateral elements and the potential is supposed to be constant on each element. More details on the theory and implementation can be found in the *PUFFIn documentation* (2023). The pressure distribution on the hydrofoil is obtained with the Bernoulli relation. Integration of the pressure over the surface S_H gives the hydrodynamic forces and moments acting on the hydrofoil.

In this work, the free surface extends 2.5 chords upstream the hydrofoil and 7.5 chords downstream. The free surface length in the spanwise direction is more than two times the hydrofoil span. A grid convergence study (not shown for the sake of brevity) was performed to select an appropriate number of panels for the hydrofoil and free surface discretization. The free surface is discretized using 140 panels in the streamwise direction and 28 panels in the spanwise direction. This ensures that a wave length corresponds to at least 20 panels. For the hydrofoil, 100 panels are used in the chord direction and 24 panels are used along the span. The uncertainty on the lift coefficient, computed using the GCI method (Roache, 1994), is estimated to be 3.5% for the converged mesh. This level of uncertainty is considered sufficient for the present study.

3.2 3D Finite Element Model of the Foils

To compute the structural response of the foil, two finite element models are considered. In this Section, the 3D finite element model of the foil, referred to as *Abaqus 3D* in the paper, is presented.

In the 3D Abaqus FEA, the foil is decomposed in two parts, a first one containing the Airex foam, meshed with 3D solid elements. The second part is meshed with 2D shell elements and represents the composite skin of the foil. The 2D shell elements used to model the UD and taffeta plies drastically reduce the size of the mesh, because the skin is not discretized throughout its thickness. The 3D solid elements used to model the Airex web are 8 node brick elements C3D8R, see (*Abaqus Theory Guide* 2022). A mesh sensitivity analysis has been performed to provide the optimal number of elements to correctly capture the behavior of the foils. The optimal number of solid elements to mesh the web is approximately 700 000 elements, such a mesh is illustrated in Figure 6. For the skin of the foil, the optimal number of elements is 60 000 (see Figure 6).

The elements used to mesh the skin are triangular Kirchhoff shell elements, denoted STRI3, see (*Abaqus Theory Guide* 2022). On these elements, a composite layup is defined to specify the thickness of the layers and the fiber orientations. A Tie constraint is also defined to link the skin to the web. This constraint imposes the surface of the web to have the same motion as the 2D skin of the foil. Finally, to model the clamping of the heel of the foil, the displacements of the skin and the web are constrained to be null in $Z = 0$ m.

The forces acting on the foil are the gravity and the hydrodynamic loading induced by the flow. The gravity loads to apply on each elements are computed in Abaqus™from the volume of the elements and the density of the materials (see Tables 2, 3).

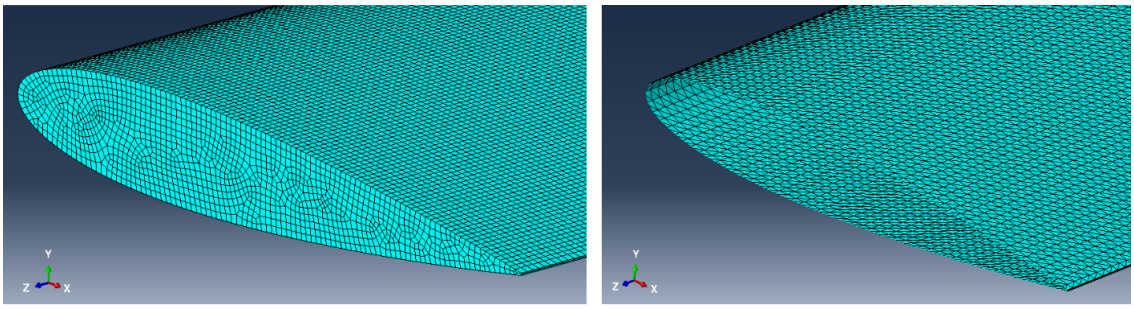

Figure 6. Structural meshes of the web of the foil (left) and of the skin of the foil (right).

3.3 1D Finite Element Model of the Foils

In this section, the 1D finite element model of the foil is presented, it is referred to as *Abaqus 1D* in the rest of the paper. To characterize the mechanical behavior of a foil with equivalent beam elements. the 3D structural problem is decomposed into a set of 2D section analysis and a 1D nonlinear FEA. To do so, the main steps are :

1. Evaluation of the structural properties of sections composing the foils (2D problems);
2. Reconstruction of equivalent beam elements;
3. 1D Finite Element Analysis (1D problem);
4. Reconstruction of 3D displacements from the results obtained with the equivalent beam model.

The first step is to characterize the structural properties of the sections along the foil span. The difficulty of this step is to find equivalent properties of an anisotropic and heterogeneous composite section. As a starting point, a 3D geometry is defined with different regions for each materials (UD, taffeta and Airex in the present work). This geometry is then cut in several sections along its span, as illustrated in Figure 7. For a prismatic foil, a single cut is required because the section is constant along its span. The number of cuts should be adapted according to the variations of the geometric and elastic properties of the foil along its span. There are 6 cuts in Figure 7 to provide a comprehensive illustration of the general method, which is not limited to prismatic foils.

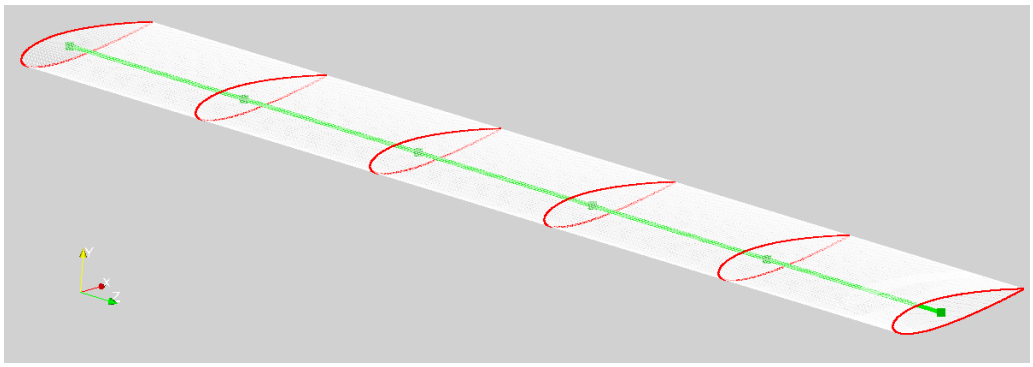

Figure 7. Illustration of the studied foil with six cuts.

A centerline has to be defined for the equivalent beam, this line goes through the shear centers of each section. The computation of the shear center is done during the next step, which is the section analysis. The shear center of the section can be computed from the terms of the compliance matrix

S, defined as the inverse of the stiffness matrix K as shown by Hodges (2006). For this step, the section is meshed and its elastic properties are integrated over its surface. The method proposed by Han and Bauchau (2015) is presently used.

Actually, two section analysis are required, a first one to compute the shear center of the section and a second one to evaluate the equivalent properties of the section at the shear center. For the first analysis, the section properties are computed according to an arbitrary origin (the leading edge of the foil in the present work). From this analysis, a first Timoshenko stiffness matrix is obtained from which the shear center is finally computed. This stiffness matrix relates the forces and moments applied on the section to its strains and curvature variations, such as:

$$\begin{pmatrix} F_1 \\ F_2 \\ F_3 \\ M_1 \\ M_2 \\ M_3 \end{pmatrix} = \begin{pmatrix} K_{11} & K_{12} & K_{13} & K_{14} & K_{15} & K_{16} \\ K_{12} & K_{22} & K_{23} & K_{24} & K_{25} & K_{26} \\ K_{13} & K_{23} & K_{33} & K_{34} & K_{35} & K_{36} \\ K_{14} & K_{24} & K_{34} & K_{44} & K_{45} & K_{46} \\ K_{15} & K_{25} & K_{35} & K_{45} & K_{55} & K_{56} \\ K_{16} & K_{26} & K_{36} & K_{46} & K_{56} & K_{66} \end{pmatrix} \begin{pmatrix} \gamma_{11} \\ \gamma_{12} \\ \gamma_{13} \\ \kappa_1 \\ \kappa_2 \\ \kappa_3 \end{pmatrix}. \tag{6}$$

The subscripts 1, 2 and 3 used in the present coordinate system (see Figure 7), are respectively related to the z, x and y directions. The matrix in Eq. 6 is representative of the equivalent mechanical properties of the analyzed cross section. K_{45} and K_{46} terms quantify the intensity and the sign of the BTC. In Abaqus™, the cross sections are meshed with triangular elements WARPF2D3, see (*Abaqus Theory Guide* 2022), that capture the anisotropic properties of the materials composing the sections of the foils. The optimal mesh is determined with a mesh sensitivity analysis where the cell sizes are decreased until convergence of the terms of K. A converged mesh of the section is shown in Figure 8.

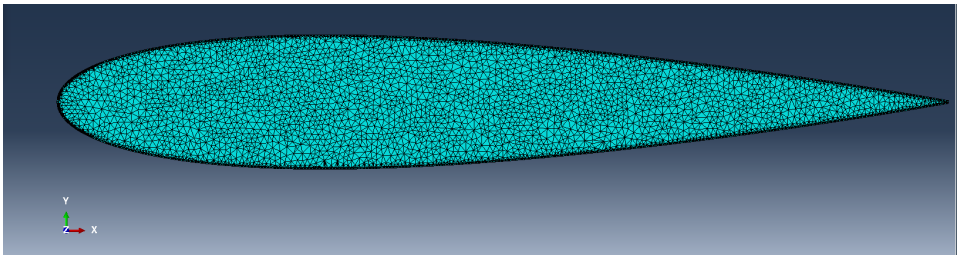

Figure 8. Triangular mesh of the cross section of a foil.

After the section analysis, beam elements are reconstructed and assembled to describe the foil as an assembly of 1D beam elements. The foil is modelled with B31 beam elements in Abaqus™, which are linear Timoshenko beam elements. The structural properties of the beam elements are determined from the section Timoshenko matrix K and the geometry (length, orientation) of the beam elements.

As in *Abaqus 3D*, the displacement of the node located in $Z = 0$ m are fixed to 0 and the loads are decomposed into a gravity component and a fluid component. To apply gravity in *Abaqus 1D*, nodes going though the centers of mass of the sections are defined, their number and position along the span are the same as the nodes of the equivalent beam elements.

The nodes going through the centers of mass are rigidly linked to their closest beam nodes and are submitted to concentrated loads corresponding to the weight of the foil. For a given node, the gravity load is computed from the lineal mass of the foil and the half-lengths of the elements linked to this nodes (only one element for the extremity nodes).

3.4 Coupling Strategies

In this Section, the coupling strategies considered to realize FSI simulations with *PUFFIn* and *Abaqus 1D* or *Abaqus 3D* are presented. The coupling strategies are similar, the differences occur when the fluid forces are transmitted to the structural solver and when the fluid mesh is deformed.

The iterative FSI coupling is explicit and Quasi-Static (QS), which means that, at each iteration, the system is considered at static equilibrium. With this kind of coupling, the acceleration of the foil and the added mass effect are not considered to compute the deformation of the foil. Figure 9 shows the organizational charts of the two couplings. The communication between the fluid and structural solver is realized with *Python* scripts.

The main steps of the two couplings are similar, the computation begin with an initial fluid computation on the undeformed geometry of the foil to determine a pressure field at the surface of the foil. Then, the iterative process begins, the deformation of the foil due to the pressure field is computed.

The static structural problem is solved using an iterative Newton-Raphson method, to take into account the non-linear geometrical effects. After the FEA, the fluid mesh is deformed according to the deformation of the foil and a new *PUFFIn* computation is performed. The two last steps are then repeated until convergence.

Two convergence criteria are defined, ϵ_s and ϵ_f, respectively for the structure and the fluid forces. ϵ_s is defined as the difference between the displacement of the tip of the foil at the current and previous iteration, u_I^{tip} is the norm of the displacement vector of the tip of the foil.

At the end of an iteration, ϵ_f is computed as the difference between the hydrodynamic force magnitude acting on the foil at the current and previous iteration. F_I is the magnitude of the fluid forces at the current iteration. A minimum number of iterations $I_{\min}$ is defined to check the convergence of the simulation. At the end of a fluid computation on a deformed foil geometry, if the number of structural iterations I is higher than $I_{\min}$ and the hydrodynamic loading and displacements of the foil are converged, the computation stops, otherwise, a new iteration is performed.

In this paper, the results presented are obtained considering ϵ_f and ϵ_s to be both equal to 0.5%. For the considered foil a typical number of iterations to reach convergence of fluid forces and displacements is about 5. At the end of the computation, the outputs are the shape of the deformed foil, the associated pressure field and the total hydrodynamic forces and moments acting on the foil.

3.4.1 Abaqus 3D

In the coupling *PUFFIn*/*Abaqus 3D*, the pressure field given by PUFFIn is applied on the surface of the foil. Because the fluid mesh is coarser than the structural mesh, the pressure field given by *PUFFIn* is interpolated on the Abaqus mesh with a distance weighting algorithm.

After the FEA, *Abaqus 3D* returns the displacement field of the surface of the foil expressed at the nodes of the structural mesh. Because this mesh does not match with the fluid one, a second interpolation is realized. Radial Basis Function (RBF) is used to compute the displacements of the fluid mesh nodes from the displacements of the structural mesh nodes.

Each structural computation in Abaqus™ begins considering a structural mesh of the undeformed foil. Therefore, the pressure field interpolated on the nodes of the structural mesh has to be expressed on the nodes of the undeformed fluid mesh. To do so, after the computation of a pressure field on a deformed geometry in *PUFFIn*, the pressure values on each faces are transported to their corresponding faces on the initial fluid mesh.

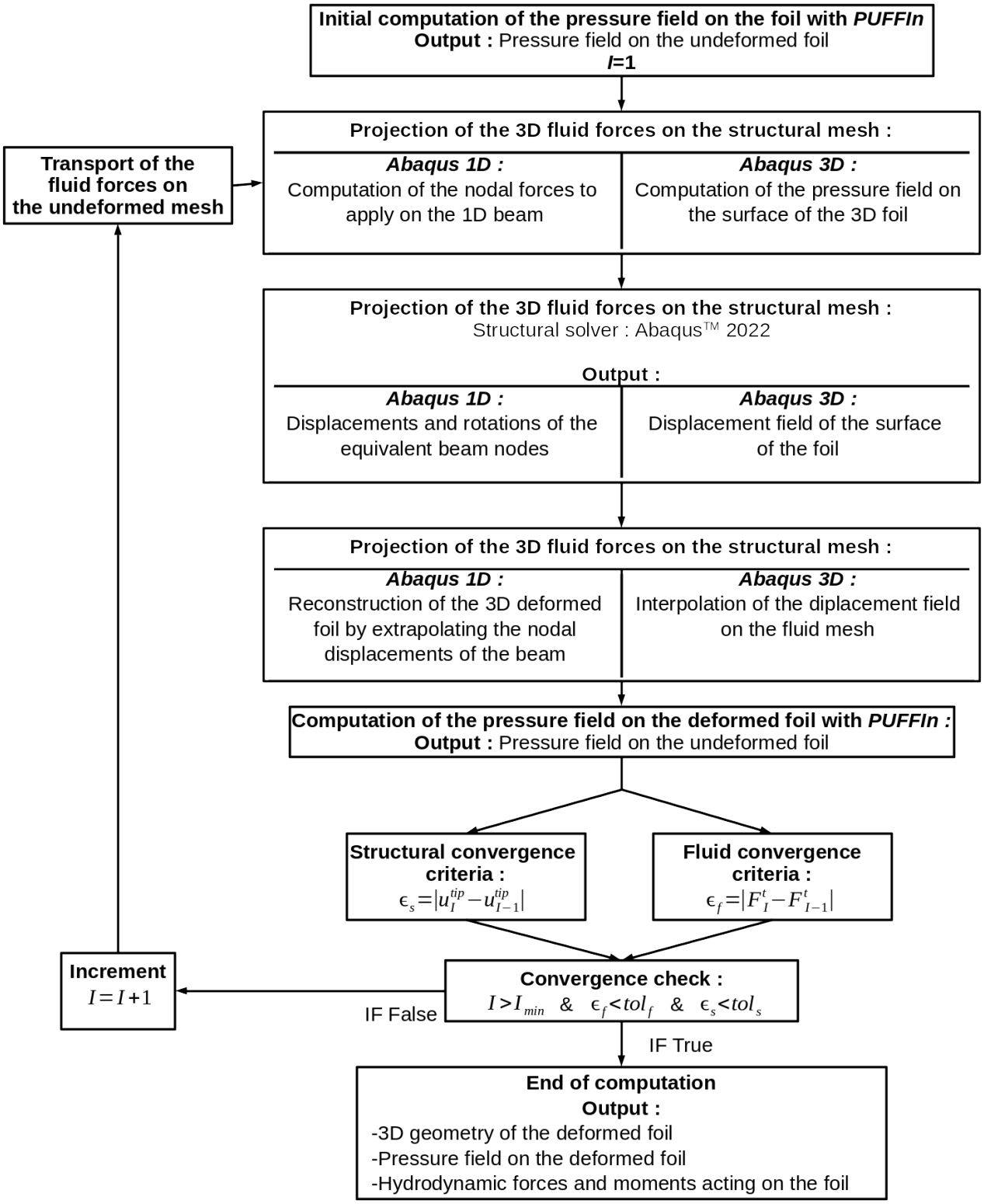

Figure 9. Organizationnal chart of the couplings *PUFFIn*/*Abaqus 3D* and *PUFFIn*/*Abaqus 1D*.

3.4.2 Abaqus 1D

In the coupling *PUFFIn*/*Abaqus 1D*, a 3D pressure field is projected on the equivalent beam elements. To do so, the pressure field is expressed as concentrated forces from the centers, the area vectors and the pressure at the fluid faces. Then, for each application point of the concentrated forces, the

closest beam element is determined. The concentrated force is distributed on the two nodes of the corresponding beam element.

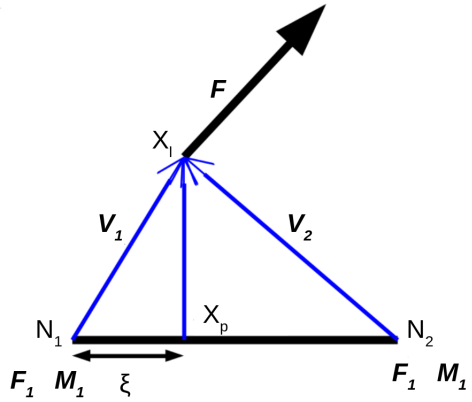

Figure 10. Illustration of the force projection method.

Figure 10 illustrates the projection method, where the beam element is defined between the nodes N_1 and N_2 and a concentrated force $\boldsymbol{F}$ is applied at point $\mathrm{X_l}$. The point $\mathrm{X_p}$ is defined as the projection of $\mathrm{X_l}$ on the beam element, $\mathrm{X_p}$ is used to define the non-dimensionnal parameter ξ used to distribute the load on the nodes N_1 and N_2 (see Eq. 7).

$$\xi = \frac{\|\overrightarrow{\mathrm{N_1X_p}}\|}{\|\overrightarrow{\mathrm{N_1N_2}}\|} \tag{7}$$

The concentrated force $\boldsymbol{F}$ is distributed between the nodes of the beam element accordingly to the value of ξ. In Figure 10, $\boldsymbol{F_1}$ and $\boldsymbol{F_2}$ are the nodal loads respectively applied on N_1 and N_2 during the FEA. The nodal forces are defined as:

$$\boldsymbol{F_1} = (1-\xi)\boldsymbol{F}, \tag{8}$$

and

$$\boldsymbol{F_2} = \xi\boldsymbol{F}. \tag{9}$$

To compute the nodal moments, defined as $\boldsymbol{M_1}$ and $\boldsymbol{M_2}$ in Figure 10, the vector $\boldsymbol{V_1}$ and $\boldsymbol{V_2}$ are respectively defined as $\overrightarrow{\mathrm{N_1X}}$ and $\overrightarrow{\mathrm{N_2X}}$. The nodal moments are computed such as :

$$\boldsymbol{M_1} = \boldsymbol{V_1} \wedge \boldsymbol{F_1}, \tag{10}$$

and

$$\boldsymbol{M_2} = \boldsymbol{V_2} \wedge \boldsymbol{F_2}. \tag{11}$$

The nodal moments and forces are non-follower, which means that their orientation is constant during the FEA. To avoid any problem of fluid faces overlapping several beam elements, the fluid mesh is refined according to the 1D structural mesh before the beginning of the iterative FSI loop. To do so, 2D planes perpendicular to the centerline of the beam elements are defined at the beam nodes. The faces of the fluid mesh intersected by these plane are cut in sub-faces in order to have a correct projection of the fluid forces on the beam elements.

After the computation of the static deformation of the foil, the fluid mesh is deformed accordingly. To do so, the shape of the deformed 3D foil is extrapolated from the nodal displacements of the beam computed during the FEA. To reconstruct a 3D deformed geometry, each of its points is projected on the closest beam element. During the projection of a point of the 3D geometry on a beam elements, two cases can be encountered:

1. The point is projected on a node of a beam element $\rightarrow$ its displacement is computed from the associated nodal displacement;
2. The point is projected on an arbitrary point of a beam element $\rightarrow$ its displacement is computed from the displacements of the nodes of the associated beam element with the linear shape functions of a Timoshenko beam element, see (Oñate, 2013).

With this approach, the sections of the foil have a rigid body motion and their deformations are not considered to reconstruct the deformed shape of a foil.

As in the coupling *PUFFIn*/*Abaqus 3D*, the structural computations always begin with the foil in its undeformed configuration. Therefore, the pressure forces projected on the foil have to be expressed on the undeformed mesh of the foil. To do so, the points of application of the forces ($\mathrm{X_1}$ in Figure 10) are considered constant during the FSI loop and they are equal to the centers of the faces of the undeformed fluid mesh. However, the forces $\boldsymbol{F}$ are computed from the current fluid mesh, which means that their orientations change when the foil is deformed. With this method, the concentrated loads applied on the beam elements are rigorously equivalent to the pressure forces computed by *PUFFIn* on a deformed fluid mesh.

4 RESULTS AND DISCUSSION

4.1 Fixed Depth

In this Section, the behavior of the foil is studied experimentally for two flow velocities, $U = 0.8$ m/s and $U = 1.2$ m/s. The depth of the foil is chosen to minimize the free surface effects. In the flume tank, the maximal depth achievable by the hexapod is $h/c = 2.76$ which corresponds to a submergence of 0.69 m for the considered foil. At this depth, the foil is 1.3 m above the flume floor, which is approximately 5.2 chords. Considering the maximal velocity $U = 1.2$ m/s and the distance of the foil to the flume floor, the work of Faltinsen (2005) shows that the expected variation of the lift coefficient due to ground effect is negligible. Thus, the flume floor is not modeled in *PUFFIn* and its impact is not discussed in this paper.

The objective is to study the behavior of the foil for several angles of attack for the two considered flow velocities. The hydrodynamic forces are computed thanks to the balance fixed to the hexapod (see Section 2.2). The forces computed on the foil are relative to the configuration where the foil is immersed in the flume tank without any current. This means that the force values presented in this

Section do not take into account the buoyancy of the foil. In the numerical models, *PUFFIn* computes the dynamic pressure forces at the last fluid iteration of the FSI loop. The values obtained do not take the buoyancy into account and thus, they are compared with the experimental measurements.

In addition to the hydrodynamic forces, the vertical displacement and torsion angle induced by the flow are also measured. The measured displacement and torsion of the foil are also relative to the reference configuration without any flow, meaning that the measured displacements are only induced by the dynamic pressure of the fluid and not the buoyancy of the foil.

Two computations are performed for each model, a first one without flow velocity and a second one with flow velocity. A value of displacement relative to the reference configuration (where the foil is only subjected to its buoyancy) is obtained by subtracting the displacement computed with flow velocity with the displacement computed without flow velocity.

The values of the relative displacements computed experimentally and numerically are plotted for different values of α in Figure 11.

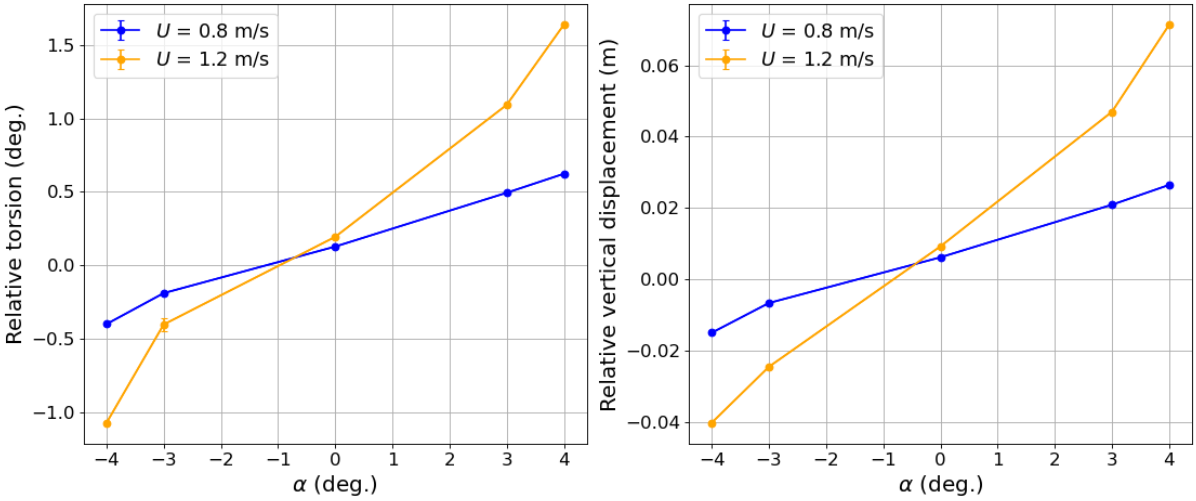

Figure 11. Experimental values of the torsion (left) and vertical displacement (right) of the foil at $h/c = 2.76$.

Figure 11 shows that for $\alpha = 0°$, the displacement and torsion of the foil are not null. This is because the foil is initially bent because of its buoyancy. Because of the BTC, the flexion of the foil due to buoyancy induces a torsion angle which increases the angle of attack of the foil. Therefore, for $\alpha = 0°$, the buoyancy of the foil induces a positive α. This is why the angle for which the displacements are null is negative. To have no deformations of the foil, its initial angle of attack must be negative in order to compensate the positive angle of attack due to buoyancy.

Figure 12 shows the impact of a nose-up twist angle on the behavior of the foil. The nose-up twist angle tends to increase the lift coefficient of the foil as it is deformed. To highlight this, the ratio between the lift coefficient for $\alpha = 4°$ and $\alpha = 3°$ can be compared to the theoretical ratio considering no nose-up twist angle. If there is no nose-up twist angle, the lift coefficient remains constant when the foil is deformed. For small values of α, the lift coefficient is assumed to be a linear function of α. The vertical displacement of the foil is also considered to be a linear function of the lift. Therefore, an increase of 33% is expected when α goes from 3° to 4°. However, for $U = 1.2$ m/s, the increase is about 52%, this is due to the nose-up twist angle, which increases the lift coefficient of the foil when it is deformed. This phenomenon is less clearly visible for the velocity of 0.8 m/s because the hydrodynamic loads induced by the flow are lower and therefore the deformation of the foil is lower.

Figure 12 shows the values of the hydrodynamic forces acting on the foil for the two velocities con-

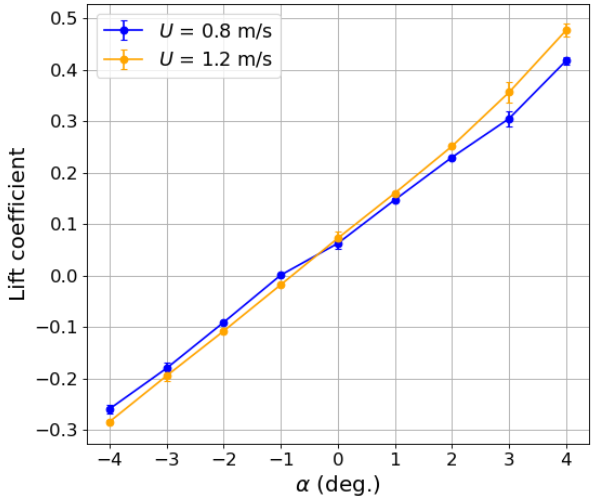

Figure 12. Experimental values of the lift coefficient of the foil at $h/c = 2.76$.

sidered. The zero lift angle of attack is negative despite the symmetry of the profile. As explained earlier, a positive angle of attack is induced by the bending due to the buoyancy of the foil.

In Figure 12, the lift coefficient magnitude is higher for the speed of 1.2 m/s. Because the lift is higher for the velocity of 1.2 m/s than for the velocity of 0.8 m/s, the flexion of the foil is more bent, resulting in a higher value of α because of the BTC. This phenomenon is more visible for high values of α, because they lead to larger deformations and thus the BTC induces a more significant nose-up twist angle.

The results show the impact of the nose-up twist angle, which leads to higher lift coefficients for the velocity of 1.2 m/s, if the lift induces a sufficient deformation. The nose-up twist angle also increases the deformation of the foil, whereas it would be decreased if the sign of the BTC was opposite.

4.2 Influence of the Immersion

In this Section, the influence of the immersion of the foil on its lift and deformation is investigated for a fixed value of α. To maximize the deformation of the foil, the value of α is set at 4° is considered. With the hexapod of the Ifremer flume tank, the immersions of the foil are fixed at $h/c = [0.5; 0.75; 1; 2.76]$.

Figure 13 shows the influence of the immersion of the foil on the lift coefficients. The effect of the free surface on the foil is different for the two considered velocities. For the lower Froude configuration ($U = 0.8$ m/s), the lift coefficient increases as the immersion decreases, until $h/c = 1$, which corresponds to the point where the wave created by the foil surges. Then, there is a major loss of lift. For the higher Froude configuration($U = 1.2$ m/s), the lift is reduced when the foil is getting near the free surface. As for the velocity of 0.8 m/s, a major loss of lift occurs when h/c is lower than 1, which reflects the surge of the free surface above the foil. The reduction of the lift is higher for $U = 1.2$ m/s because the associated surge is more important.

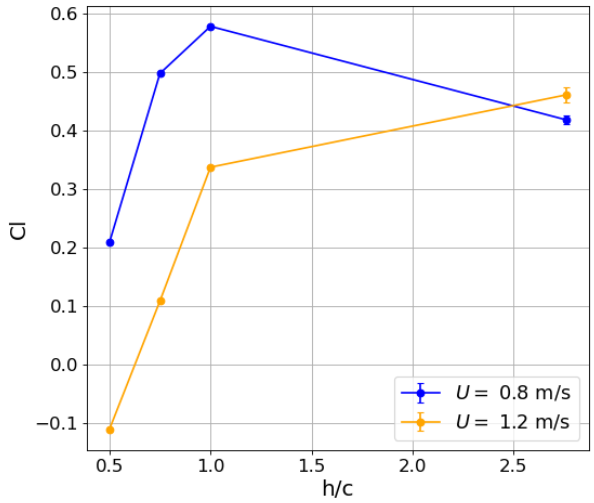

Figure 13. Experimental values of the lift coefficient for $\alpha = 4°$.

Figures 14 show the experimental measures of torsion and vertical displacement of the foil as a function of the immersion of the foil. As in Section 4.1, the torsion and vertical displacement follows similar tendencies, which can be related to the lift of the foil. The results show that the deformation of the foil far from the free surface are higher for the velocity of 1.2 m/s, which is expected because the lift is higher in this case. For the lower Froude configuration, Figure 14 shows that the vertical displacement is maximum for $h/c = 1$, which is consistent with the evolution of the lift coefficient presented in Figure 13. A similar observation can be done for the higher Froude configuration, where the deformation of the foil are maximum for $h/c = 2.76$ and decreasing when it is closer to the free surface. Figure 14 also show the loss of lift for low immersion, resulting in an important reduction of the deformation of the foil.

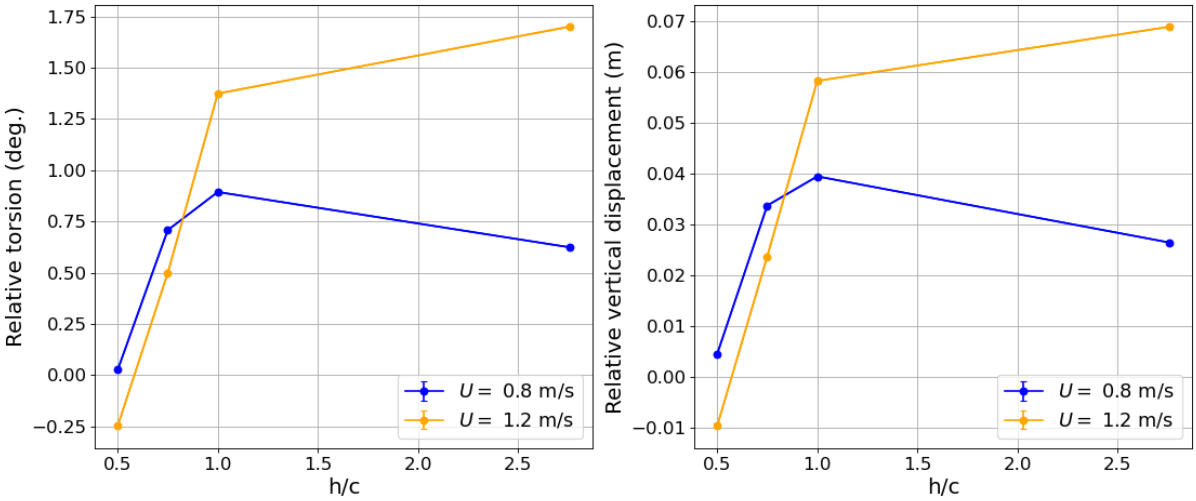

Figure 14. Experimental values of the torsion and vertical displacement of the foil for an $\alpha = 4°$.

The experimental measures show that the behavior of the foil near the free surface is Froude-dependent. For the lowest Froude configuration, an increase of the lift of the foil occurs when it is getting closer to the free surface, this phenomenon is due to an augmentation of the depression at the extrados of the foil, which disappears when the free surface above the foil surges. For the higher Froude configuration, the lift increases with the immersion and, as for the lower Froude configuration, there is a major loss of lift for low immersion, which corresponds to the surging of the wave induced by the foil.

4.3 Validation of Numerical Models

In this section, results obtained with the numerical models are compared to the experimental results. The foil is tested for the maximum immersion ($h/c = 2.76$) and a velocity of $U = 0.8$ m/s. Various values of α have been tested, from -4° to 4°. Figure 15 shows the torsion and vertical displacements computed numerically and experimentally.

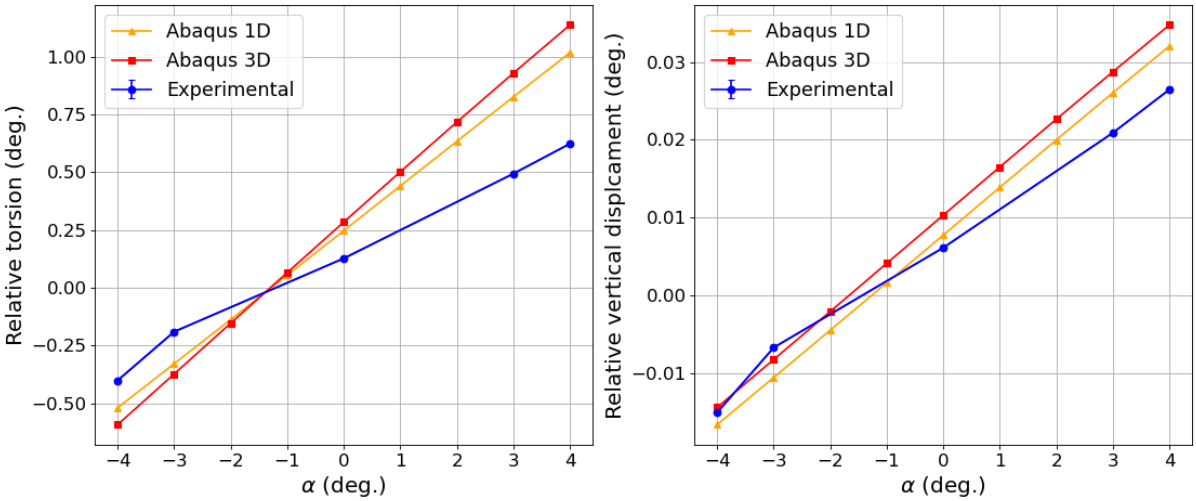

Figure 15. Experimental and numerical values of the torsion (left) and the vertical displacement (right) of the foil at $h/c = 2.76$.

The results show that the two numerical models give similar results. This validates that 3D composite foils can be modelled with 1D beam elements, instead of 3D solid and 2D shell elements, which are commonly used. Such results are expected, as seen in Faye et al. (2022), where the equivalent beam approach is validated for concentrated load cases.

The numerical models both overestimate the deformation of the foil. Figure 15 shows that the difference on the torsion between the numerical model and the experiment is higher than the difference on the vertical displacement. This could be caused by an over-estimation of the BTC. This would explain why the difference on the torsion is higher than the difference on the vertical displacement. To illustrate the difference on the BTC between the experiments and the numerical models, the torsion is plotted as a function of the vertical displacement, giving a linear curve with a slope proportional to the BTC of the foil. The slope of the the curve is referred to as the Bend Twist Ratio (BTR) in the rest of the paper and its numerical value is denoted β. Results showing the BTC estimation are plotted in Figure 16.

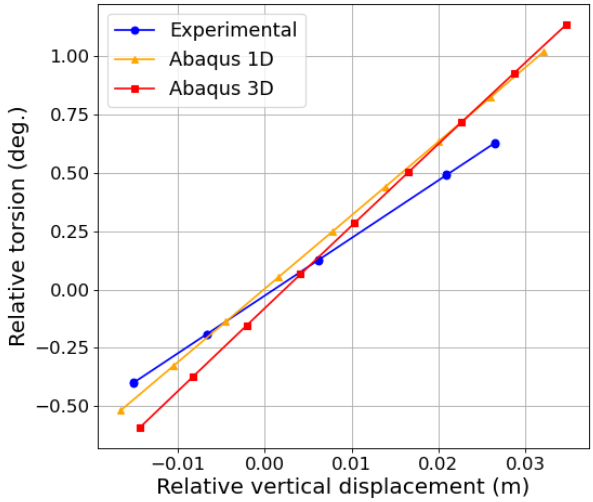

Figure 16. Experimental and numerical bend-twist coupling.

In Figure 16, the slope of the curve relative to the experiments is slightly lower, the values of the different BTR are gathered in Table 4, where β_{exp} is the BTR computed from the experimental results. Considering that the slopes are representative of the BTC, the results shows that the BTC is lower in the experiments than in the numerical models.

When computing the ratio between the experimental and numerical BTC, a mean value of 0.74 is found. This value can be used to reduce the BTC in the numerical model *Abaqus 1D*. To do so, the term K_{45} of the Timoshenko stiffness matrix of the section (see Eq. 6) is multiplied by 0.74. Because of the uncertainties on the manufacture of the experimental foil, it is possible that the composite layup defined during the section analysis (and in *Abaqus 3D*) does not perfectly match the real structure. Moreover, the BTC term K_{45} is very sensitive to small structural variations (orientation of the UD, composite layup engineering constants) and therefore, the equivalent stiffnesses could be computed correctly but not the BTC.

Table 4. Experimental and numerical value of the bend-twist ratio.

Model	β (deg./m)	$\frac{\beta_{\text{exp}}}{\beta}$
Experimental	24.7	1.00
Abaqus 3D	31.6	0.78
Abaqus 1D	35.2	0.70

The FSI simulations with the coupling *PUFFIn*/*Abaqus 1D* are relaunched with a lower BTC coefficient, its original value is reduced by 26%. The new results on the torsion and vertical displacement are given in Figure 17.

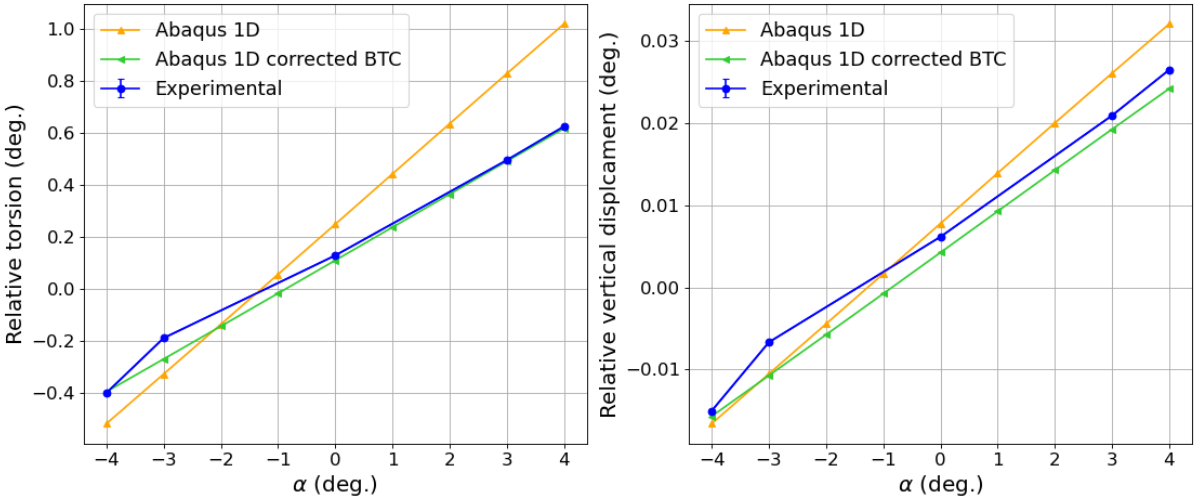

Figure 17. Experimental and numerical values of the torsion (left) and vertical displacement (right) of the foil at $h/c = 2.76$, after correction of the BTC.

After correction of the numerical BTC in *Abaqus 1D*, the slopes and magnitude of the displacement and rotations are closer to the experimental values. Except for the $\alpha = -3°$, the fit between experimental and numerical values is good, this shows the impact of the BTC on the hydroelastic response of the foil. The forces coefficient computed experimentally and numerically are plotted in Figure 18.

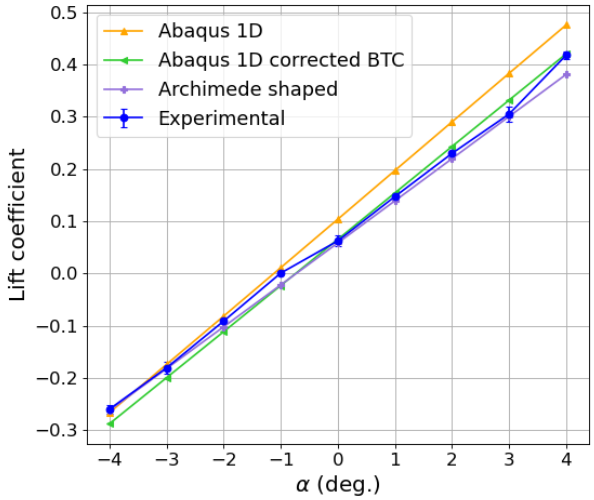

Figure 18. Experimental and numerical values of the lift coefficient of the foil at $h/c = 2.76$, after correction of the BTC.

There is a good match for $\alpha >= 0°$ but for $\alpha < 0°$, the model without correction fits better the experiments. The major difference between the experimental and numerical results is the trend of the lift coefficients. In the numerical model, the curve is monotonic whereas the experimental curve shows a change of trend between $\alpha = -1°$ and $\alpha = 0°$. After analysing the experimental data, an explanation to this would be a problem with the measurement of the forces acting on the foil without any current, probably because of the effects of drift of the balance.

In Figure 18, there is also the lift coefficients obtained on a rigid foil. Because the reference configuration in the experiments is the foil submitted to its buoyancy only, the *Archimede shaped* computations are realized with a mesh of the shape of the foil deformed by its buoyancy (considering the corrected

value of the BTC coefficient). The *Archimede shaped* results highlights the effect of the BTC on the lift of the foil. The slope of the C_l curve is higher in the FSI simulations than in the *Archimede shaped* computations, meaning that, at a given angle of attack, the deformation of the foil tends to increase its lift. This is due to the BTC which increases the angle of attack of the foil when it is deformed, and therefore it increases its lift.

In Figure 18, the zero-lift angle of attack are always negative, this is because at 0°, the foil has a positive angle of attack induced by the buoyancy and the BTC. Thus, to have zero lift, the initial angle of attack of the foil has to be negative in order to compensate the angle of attack induced by the buoyancy.

Finally, Figure 19 illustrates the shape of the deformed foil obtained numerically. The pressure field on the foil is plotted on the initial shape of the foil and on its deformed shape. Figure 19 shows lower pressure coefficients on the extrados of the foil in its deformed configuration, highlighting the additional angle of attack of the foil induced by the BTC.

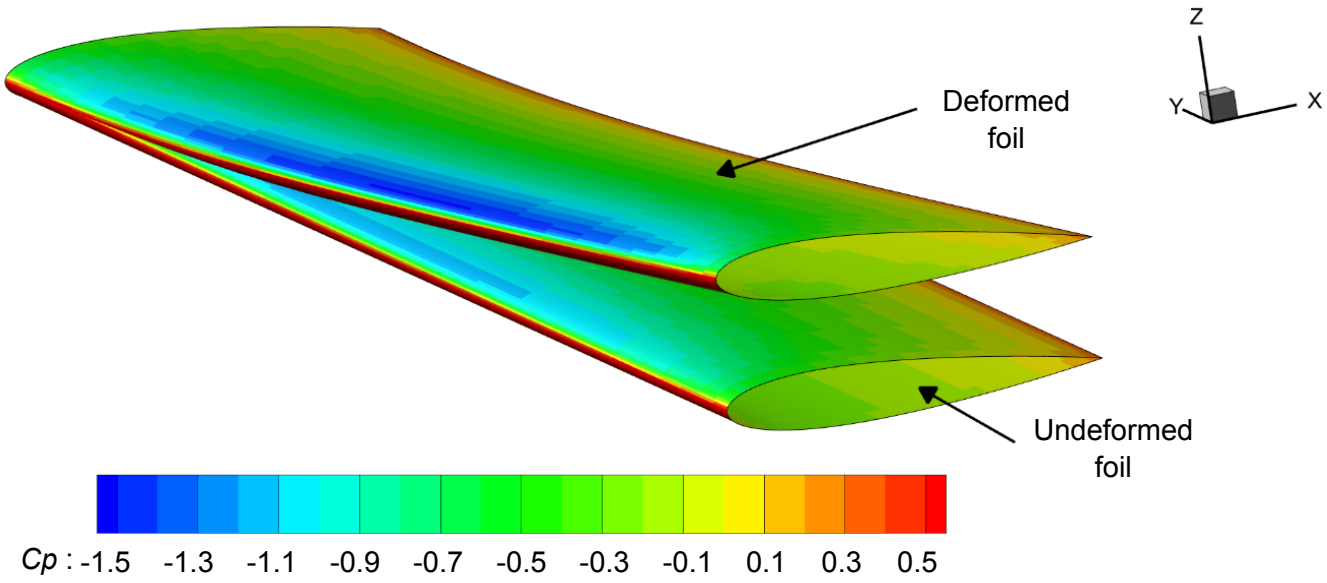

Figure 19. Pressure fields at the surface of the foil computed on its initial shape and deformed shape, for $\alpha = 4°$, $h/c = 2.76$ and $U = 0.8$ m/s.

To sum up the numerical results, it is shown that the model *Abaqus 1D* is equivalent to *Abaqus 3D*, which validates that equivalent beam finite elements can be used to describe the structure of composite foils. In addition to that, the experimental results shows that the numerical BTC is overestimated and a reduction of this coefficient by 26% is required to fit the numerical results to the experiments. The computation of the BTC (K_{45}) during the section analysis is very sensitive to the composite layup defined in Abaqus ™. For instance, a variation of 1° of the UD orientation and 5% of the young modulus leads to a 7% variation of the value of K_{45}. The equivalent beam method is suited to describe the hydroelastic response of a foil but a precise modelization of the BTC is mandatory in order to have consistent results.

5 CONCLUSIONS

In this paper, the hydroelastic behavior of a foil submitted to hydrodynamic loads was investigated both numerically and experimentally. Experimental measurements on the foil were realized at the Ifremer flume tank in Boulogne-sur-mer, for two velocities, four immersion and several angle of attacks. The foil studied presents a BTC inducing a nose-up twist angle when it is deformed. This means that the

hydrodynamic loads acting on the foil increases when it is deformed. This phenomenon is captured experimentally for the two velocities considered, showing the impact of the BTC in FSI of composite foils.

Subsequently, the influence of the immersion of the foil is investigated experimentally. For the two Froude number considered, different behaviors are observed. The higher Froude configuration shows a reduction of the lift coefficients when the foil gets closer to the free-surface. For the lower Froude configuration, the lift coefficient increases as the immersion of the foil is decreasing, until the wave of the foil surges, causing a major loss of lift.

In this study, two different coupled numerical approaches are presented to simulate the FSI of the foil. For both FSI coupling, the hydrodynamic forces of the foil are computed with the BEM, as implemented in *PUFFIn*. For the first numerical model (*Abaqus 3D*), the structure of the composite foil is studied with 3D solid elements and 2D shell elements. For the second FSI coupling (*Abaqus 1D*), the foil is modelled with 1D finite element equivalent to the 3D model. This method requires a preliminary evaluation of the cross-sections of the foil, which determines the equivalent stiffness of the foil and the potential couplings in the material, such as the BTC.

The numerical results obtained with *Abaqus 3D* and *Abaqus 1D* show a good agreement, which confirms that equivalent beam elements can be used to model the composite foil, resulting in a major reduction of the computational time. This also validates the method used to project the 3D pressure forces (computed in *PUFFIn*) onto the 1D equivalent beam elements.

At the end of the paper, a validation of the numerical models is presented, considering the experimental measurements as reference values. The comparison shows that the BTC of the numerical models is overestimated, resulting in higher values of α and therefore higher deformation and lift coefficients. A reduction of the BTC of 26% in the numerical model is proposed based on the difference between numerical and experimental results. After the correction, the fit between experimental and numerical results is greatly improved. This highlights the sensitivity of the BTC to the composite layup in the numerical models. Small uncertainties on the material and its orientation may leads to significant variations of the BTC.

The numerical model presented in this paper can be used to study the hydroelastic responses of composite hydrofoils. However, a rigorous description of its structures is mandatory in order to model correctly the couplings in the material.

As future work, an investigation of the structure of the foil is studied to identify precisely the difference in the numerical models leading to an overestimated BTC. Another perspective is to study a foil with an opposite BTC coefficient, in order to have nose-down twist angle induced by the flexion of the foil.

6 ACKNOWLEDGMENTS

The authors would like to thank the Ifremer of Boulogne-sur-Mer (France), which made this experiments possible. Finally, we also want to acknowledge Jean-Baptiste Marchand of the company Mabe surfboards for the manufacturing of the foils.

REFERENCES

Abaqus Theory Guide (2022). Providence, RI: Dassaut Systèmes.

Faltinsen, O.M. (2005). *Hydrodynamics of High-Speed Marine Vehicles*. Cambridge University Press, pp. 165–220.

Faye, A., Carrere, N., Sacher, M., Hauville, F., and Nême, A. (2022). Determination of the equivalent structural properties of a composite hydrofoil. *Congrès Français de Mécanique 2022*. Nantes, France.

Graf, K., Freiheit, O., Schlockermann, P., and Mense, J. (2021). VPP-Driven Sail and Foil Trim Optimization for the Olympic NACRA 17 Foiling Catamaran. *Journal of Sailing Technology* 5, pp. 61–81. DOI: 10.5957/jst/2020.5.1.61.

Han, S. and Bauchau, O. (2015). Nonlinear Three-Dimensional Beam Theory for Flexible Multibody Dynamics. *Multibody System Dynamics* 34. DOI: 10.1007/s11044-014-9433-8.

Hodges, D. (2006). *Nonlinear Composite Beam Theory*. AIAA. ISBN: 978-1-56347-697-6. DOI: 10.2514/4.866821.

Katz, J. and Plotkin, A. (2001). *Low-speed aerodynamics*. Vol. 13. Cambridge university press.

Liao, Y., Garg, N., Martins, J., and Young, Y. L. (2019a). Viscous Fluid Structure Interaction Response of Composite Hydrofoils. *Composite Structures* 212. DOI: 10.1016/j.compstruct.2019.01.043.

Liao, Y., Martins, J., and Young, Y. L. (2019b). Sweep and Anisotropy Effects on the Viscous Hydroelastic Response of Composite Hydrofoils. *Composite Structures* 230, p. 111471. DOI: 10.1016/j.compstruct.2019.111471.

Liao, Y., Martins, J., and Young, Y. L. (2021). 3-D High-Fidelity Hydrostructural Optimization of Cavitation-Free Composite Lifting Surfaces. *Composite Structures* 268, p. 113937. DOI: 10.1016/j.compstruct.2021.113937.

Liao, Y., Martins, J., and Young, Y. L. (2023). Hydrostructural optimization of single-layer and multilayer composite lifting surfaces. *Composite Structures* 307, p. 116650. DOI: 10.1016/j.compstruct.2022.116650.

Lottati, I. (1985). Flutter and divergence aeroelastic characteristics for composite forward swept cantilevered wing. *Journal of Aircraft - J AIRCRAFT* 22, pp. 1001–1007. DOI: 10.2514/3.45238.

Marimon Giovannetti, L., Farousi, A., Ebbesson, F., Thollot, A., Shiri, A., and Eslamdoost, A. (2022). Fluid-Structure Interaction of a Foiling Craft. *Journal of Marine Science and Engineering* 10, p. 372. DOI: 10.3390/jmse10030372.

Marty, A., Berhault, C., Guillaume, D., Facq, J.V., Gaurier, B., Germain, G., Soulard, T., and Schoefs, F. (2021). Experimental study of hard marine growth effect on the hydrodynamical behaviour of a submarine cable. *Applied Ocean Research* 114, p. 102810. DOI: 10.1016/j.apor.2021.102810.

Mohammed Arab, F. (2020). Contrôle actif par pression interne des performances hydrodynamiques et de l'apparition de la cavitation d'un hydrofoil composite déformable en composite. PhD Thesis. UBO.

Newman, J. N. (2018). *Marine hydrodynamics*. The MIT press.

Oñate, E. (2013). *Structural analysis with the finite element method. Linear statics. Volume 2: Beams, plates and shells*. Vol. 2. Springer.

Patterson, N. and Binns, J. (2022). Development of a Six Degree of Freedom Velocity Prediction Program for the foiling America's Cup Vessels. *Journal of Sailing Technology* 7, pp. 120–151. DOI: 10.5957/jst/2022.7.6.151.

PUFFIn documentation (2023). https://www.ensta-bretagne.fr/fe/optifoil.

Roache, P.J. (1994). Perspective: A Method for Uniform Reporting of Grid Refinement Studies. *Journal of Fluids Engineering-transactions of The Asme - J FLUID ENG* 116, pp. 405–413. DOI: 10.1115/1.2910291.

Temtching Temou, V. (2020). Etude expérimentale et numérique des interactions fluide-structure sur des hydrofoils flexibles en composite. PhD Thesis. UBO. URL: http://www.theses.fr/2020BRES0043/document.

Young, Y. L., Garg, N., Brandner, P., Pearce, B., Butler, D., Clarke, D., and Phillips, A. (2017). Load-Dependent Bend-Twist Coupling Effects on the Steady-state Hydroelastic Response of Composite Hydrofoils. *Composite Structures* 189. DOI: 10.1016/j.compstruct.2017.09.112.